Green Fabrication of Heterostructured CoTiO₃/TiO₂ Nanocatalysts for Efficient Photocatalytic Degradation of Cinnamic Acid

Cam Anh Ha,* Dien Trung Nguyen, and Tri Nguyen

Read Online

ACCESS | Metrics & More | Article Recommendations

ABSTRACT: In this work, $CoTiO_3/TiO_2$ (CTO/Ti) heterostructures were prepared by a hydrothermal procedure in a neutral medium using perovskite $CoTiO_3$ and tetraisopropyl titanate. Characteristics of the synthesized catalysts were analyzed by various techniques including X-ray diffraction, Fourier transform infrared spectroscopy, Raman spectroscopy, UV−vis diffuse reflectance spectroscopy, Brunauer−Emmett−Teller adsorption−desorption, energy-dispersive X-ray spectroscopy, field emission scanning electron microscopy, high-resolution transmission electron microscopy, and point of zero charges. The activity in the photodegradation of cinnamic acid (CA) under UV-A irradiation of the CTO/Ti heterostructure was investigated and compared with individual materials TiO_2 (Ti-w) and $CoTiO_3$ (CTO). The investigation

showed that the heterostructured $CoTiO_3/TiO_2$ catalyst with optimal composition (5% CTO) exhibited much higher photocatalytic activity for degradation of cinnamic acid than individual $CoTiO_3$ and TiO_2. Under the optimal conditions (C_{cat} = 0.75 g/L, Q_{air} = 0.3 L/min, and pH = 3.8) the 90 min conversion of cinnamic acid reached 80.9% on 5CTO/Ti, much higher than those of CTO (4.6%) and Ti-w (75.2%). It was found that the enhancement in activity for the CA removal of the CTO/Ti heterostructure was due to the construction of a heterojunction structure between TiO_2(Ti-w) and $CoTiO_3$ that resulted in an increase in the specific surface area and porosity, reduction of the band gap energy, and higher efficient separation of charge carriers on the surface to prevent recombination. Alternatively, a comparison of the recyclability of 5CTO/Ti and Ti-w was made for CA degradation. The results showed a decrease in the CA conversion by 38% on 5CTO/Ti and 48% on Ti-w after six reaction cycles.
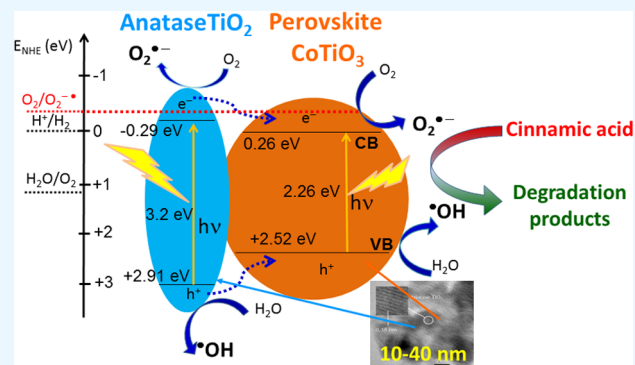
INTRODUCTION

Phenolic compounds belong to one of the largest groups of pollutants because of their wide applications in the agro-industrial sector and as antimicrobial agents.[1] Due to their high toxicity and nonbiodegradability the phenolic compounds are defined as priority pollutants. Thus, the treatment of wastewater containing phenolic compounds is critical to the sustainability of water resources. Among the phenolic compounds, cinnamic acid (CA) is one of the important intermediates in organic synthesis as well as widely used in the manufacture of drugs, pesticides, resins, and photosensitive resins.[2] In particular, wastewater from olive factories and wineries contained a lot of phenolic acids and polyphenols, mainly derivatives of benzoic acid and cinnamic acid.[3,4] The concentration of toxic and persistent CA present in wastewater from olive oil factories can reach 106 mg/L.[5] Photocatalytic oxidation has received increasing attention for removing organic pollutants in water due to its high efficiency, low energy consumption,[6] and the ability to completely mineralize the organic pollutants into carbon dioxide and water at room temperature and atmospheric pressure.[7]

Among the various photocatalysts for wastewater treatment, metal oxide TiO_2 (Ti) was generally considered the best and widely used commercially due to its natural abundance, nontoxicity, low cost, and high corrosion resistance.[8,9] However, the limitation of light-harvesting ability, the easy recombination of electron−hole pairs, and the low surface area caused a decrease in the photocatalytic efficiency.[10] Graphene oxide has received attention for improving photocatalytic performance. TiO_2 combined with graphene oxide exhibited high photocatalytic activity for pollutants owing to the increased surface area.[11,12] Additionally, titanium-based perovskite $MTiO_3$ (M = Fe, Co, and Ni) has been pointed out as a promising candidate for photoactive materials[13,14] due to its low band gap energy. Recently, $CoTiO_3$ (CTO) has received
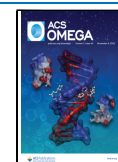
much attention thanks to its narrow band gap energy (E_g = 2.25 eV), strong visible-light absorption, outstanding photochemical stability, and low cost.[15]

Subsequently, the combination of TiO$_2$ with perovskite titanate to form a heterostructure has been developed to improve the photocatalytic performance based on a synergistic effect to transfer charges efficiently, enhance light harvesting, and stability.[16−19] SrTiO$_3$/TiO$_2$ nano-heterostructures enhance the charge separation hole-transportation and visible-light-driven photocatalytic performance over TiO$_2$.[20] Combination TiO$_2$ with visible-light-sensitized NiTiO$_3$ has significantly enhanced the surface area, light absorption, and charge separation for photocatalytic hydrogen evolution.[21,22] Attaching a small amount of NiTiO$_3$ to TiO$_2$ reduces the particle size and average crystallite size (8.6 vs 34.8 nm) and lowers the band gap energy (3.02 vs 3.20 eV). The mixed catalysts enable a red-shift in the absorption band from UV (λ = 385 nm) to UV-A light (λ = 404−412 nm) that improved the activity of the catalyst in CA photodegradation.[23]

In some studies, TiO$_2$ was combined with pseudobrookites such as Fe$_2$TiO$_5$[24,25] or Al$_2$TiO$_5$[26] to construct heterostructure photocatalysts having high efficiency. In this work,[24] the type-II heterojunction Fe$_2$TiO$_5$/TiO$_2$ was synthesized by carbon templates and ion adsorption. The hollow nanosphere had a high surface area of 220 m^2/g and its photocatalytic activity was three times that of P25 in the degradation of rhodamine B. Meanwhile, Fe$_2$TiO$_5$/TiO$_2$[25] and Al$_2$TiO$_5$/TiO$_2$[26] heterostructures were synthesized via a simple combination of sol−gel and hydrothermal methods in a neutral medium of water. It was found that compared to TiO$_2$, the combination of TiO$_2$ with Fe$_2$TiO$_5$ and Al$_2$TiO$_5$ has significantly reduced the crystal and particle size, increased the surface area, simultaneously reduced the band gap energy of the catalyst, and extended the region of the photon absorption zone toward visible waves (407 vs 395 nm). As a result, the maximal 90 min CA conversion reached 89.0 and 76.0%, much higher than that of individual Fe$_2$TiO$_5$ (8.5%), Al$_2$TiO$_5$ (10%), and TiO$_2$ (60%). The results showed that hybridizing a small band gap perovskite or pseudobrookite and the large band gap TiO$_2$ semiconductor was a prominent approach to fabricating highly active photocatalysts.

From the review, it is observed that different methods are used in the preparation of perovskite-based materials. The citrate method is widely used in the preparation of many types of perovskites, for example, the catalytic oxide precursors MNiO$_x$ (M = La, Ce, and Sr)[27,28] and the La$_{1-x}$Ce$_x$NiO$_3$ mixed oxides[29] were prepared by the citrate method. A series of LaNiO$_3$ materials were synthesized by the ethylenediamine tetraacetic acid (EDTA)−citrate complexing method[30] and citrate sol−gel method,[31,32] while ferroelectric LaNiO$_3$ powders were prepared using an "amorphous citrate" route.[33] This method uses citric acid as a complexing agent and metallic nitrates as precursors. Several other synthesis methods are also used for the preparation of perovskites, such as the Pechini method,[34] sol−gel self-combustion method that uses citric acid monohydrate (C$_6$H$_8$O$_7$·H$_2$O) as the complexing agent, and lanthanum oxide (La$_2$O$_3$), cobalt nitrate hexahydrate (Co(NO$_3$)$_2$·6H$_2$O), nickel nitrate hexahydrate (Ni(NO$_3$)$_2$·6H$_2$O), and ferric nitrate nonahydrate (Fe(NO$_3$)$_3$·9H$_2$O) as precursors,[35] and the self-combustion method that uses metallic nitrates and glycine as a precursor for the preparation of nanocrystalline perovskites, Ce$_x$Sr$_{1-x}$NiO$_3$ (x = 0.6−1.0),[36] nanocrystals SrNiO$_3$ and CeNiO$_3$,[37][37] and

La$_{1-x}$Sr$_x$NiO$_3$ perovskite-type oxides.[38,39] Of the methods used to prepare perovskite-like materials, hydrothermal synthesis in supercritical water has advantages because the reaction rate is enhanced more than 10^3 times that under the conventional hydrothermal conditions with the products of high crystallinity and at relatively low temperatures, below 300 °C, since ionic products (Kw) have a maximum value of around 250−300 °C.[40] Hydrothermal methods for preparing fine metal oxide particles in subcritical and supercritical water have been developed using batch reaction[41−43] and flow reaction systems.[44−46]

Up to now, the combination of small band gap titanate perovskites with TiO$_2$ to create a heterostructure catalyst with efficient photocatalytic activity in the treatment of phenolic organic compounds in polluted water has been rarely studied. To our knowledge, up to now, there has been no research on synthesizing CoTiO$_3$/TiO$_2$ composites, especially by the green route and investigating its activity in the photodegradation of phenolic acids. From the above analysis, in the present work, the heterostructured catalyst CoTiO$_3$/TiO$_2$ was synthesized via the hydrothermal technique in a neutral medium. The peculiarity of this method is that it is green because water was used as the solvent in the synthesis of TiO$_2$ and mixed oxides. The structural and physicochemical characteristics of the CTO/Ti composite system were explored, and its activity and stability were tested for photocatalytic degradation of CA under UVA irradiation and compared with individual TiO$_2$ and CoTiO$_3$.

■ EXPERIMENTAL SECTION

Materials. Tetraisopropyl titanate (Ti(OC$_3$H$_7$)$_4$, Merck, 97.0%), hydrochloric acid (HCl, Prolabo, 98.0%), sodium chloride (NaCl, Merck, 99.0%), sodium hydroxide 1.0 N solution (NaOH, Pharmacopoeia Europaea), cinnamic acid (C$_9$H$_8$O$_2$, Merck, 97.0%), ethanol (C$_2$H$_5$OH, Merck, 99.5%), citric acid monohydrate (C$_6$H$_8$O$_7$·H$_2$O, Merck, 99.0%), and cobalt(II) nitrate hexahydrate (Co(NO$_3$)$_2$·6H$_2$O, Merck, 97.0%) were used in this investigation.

Synthesis of Catalysts. *Synthesis of the CoTiO$_3$ (CTO) Perovskite.* The CTO perovskite was prepared by the citrate sol−gel method. Typically, solutions containing 2.10 g of citric acid and 2.91 g of Co(NO$_3$)$_2$·6H$_2$O in 5.0 mL of ethanol under stirring for 30 min to obtain a homogeneous solution. Next, 3 mL of tetraisopropyl titanate was added to the obtained solution to form a gel. After aging overnight at room temperature, the prepared gel was dried at 60 °C for 12 h. Finally, the dried gel was calcined at temperatures in the range of 650−750 °C for 1−3 h to obtain the CTO catalyst.

Synthesis of the CoTiO$_3$/TiO$_2$ (CTO/Ti) Catalyst. The construction of the CTO/Ti composites was achieved by the hydrothermal method. In a typical synthesis, 3 mL of tetraisopropyl titanate was added to 40 mL of water under magnetic stirring for 30 min. Then, the CTO perovskite and the obtained mixture were simultaneously transferred to a 100 mL Teflon-lined stainless steel autoclave and subsequently heated at 160 °C for 12 h in an oven. After the reaction, the greenish-white precipitate was centrifuged and washed with deionized water as well as ethanol three times. The product was obtained by drying in a vacuum oven at 60 °C for 12 h and denoted as xCTO/Ti, where x is the CTO content (wt %). As a comparison, a pure TiO$_2$ catalyst, namely Ti-w, was also prepared by the same procedure using water as the solvent and without CTO.

Characterization of the Catalysts. The physicochemical characteristics of the samples were studied by several methods, which are described in detail in the article.[23] Briefly, X-ray powder diffraction (XRD) on a Bruker D2 Phaser X-Ray diffractometer with Cu Kα radiation (λ = 0.1542 nm), field emission scanning electron microscopy (FE-SEM) using Hitachi S4800, high-resolution transmission electron microscopy (HR-TEM) on a JEOL JEM 1400; energy-dispersive X-ray spectroscopy (EDS) on a JEOL JST-IT 200 instrument and the weight percent of the elements present in the xCTO/Ti catalyst composition was calculated by eq 1

$$W_i = \frac{xM_i + (100 - x)M_i}{xM_{CoTiO_3} + (100 - x)M_{TiO_2}} \times 100 \tag{1}$$

where W_i is the weight percent of the element (i = Co, Ti, and O), x is the mass percent of the CTO present in the catalyst xCTO/Ti, M_i is the mass of an element in the catalyst, M_{CoTiO_3} is the molecular weight of $CoTiO_3$, and M_{TiO_2} is the molecular weight of TiO_2.

Fourier transform infrared (FT-IR) spectroscopy in the range from 400 to 4000 cm^{-1} was carried out on a Tensor 27-Bruker spectrometer, UV−vis diffuse reflectance spectroscopy (DRS) was carried out on a Varian Cary 5000 UV-VisNIR spectrophotometer and band gap of catalyst was calculated using the general equation (eq 2)

$$\alpha h\nu = B(h\nu - E_g)^{0.5} \tag{2}$$

where E_g is the band gap (eV), h is the Planck's constant ($J \times s$), B is the absorption constant, ν is the light frequency (s^{-1}), and α is the extinction coefficient.

The specific surface area was measured on a Nova 2200e instrument and calculated with the Brunauer−Emmett−Teller (BET) model and the pore size distribution was determined using the Barrett−Joyner−Halenda (BJH) method. The point of zero charge (PZC) of the samples was determined by the salt addition method.[47]

Photocatalytic Activity. Photocatalytic activity of the synthesized samples was evaluated by CA degradation in the batch system, under ultraviolet light irradiation from 36 UV-A Engin LZ1-00 U600 lamps with $\lambda \approx 350−400$ nm, concentrated at 365 nm, as described in our previous study.[23] Briefly, the reaction solution volume is 250 mL and cinnamic acid concentration is 50 mg/L. The reaction solution was separated by filtration and analyzed using a UV-1800 (Shimadzu) UV−visible spectrophotometer at 272 nm. The effects of the operation parameters including the catalyst dosage (C_{cat} = 0.50, 0.75, 1.00, and 1.25 g/L), the initial pH of the solution (pH = 3.0, 3.8, 5.0, 7.0, and 9.0), and the airflow rate (Q_{air} = 0, 0.1, 0.3, and 0.5 L/min) were investigated. The recyclability of catalysts was tested under favorable reaction conditions for six cyclic. CA solution was removed at the end of each batch and replaced with a new CA solution to conduct the photocatalytic reactions in succession.

■ RESULTS AND DISCUSSION

Physicochemical Properties of the Obtained Materials. The thermogravimetric analysis (TGA) diagram used to investigate the thermal pyrolysis of the as-prepared CoTiO$_3$ gel is shown in Figure 1. There are four weight loss processes that could be observed in Figure 1. The first step, corresponding to 24.8% weight loss at temperatures between 30 and 200 °C with

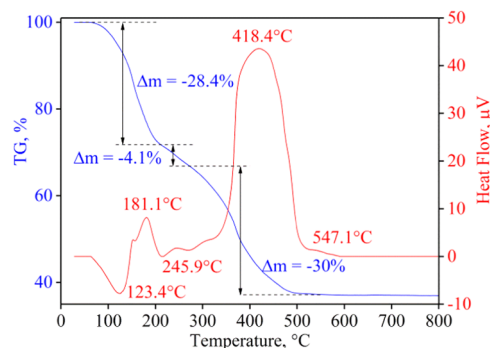**Figure 1.** TGA diagram of the as-prepared CoTiO$_3$ gel.

two temperature peaks at 123.4 and 181.1 °C, is assigned to the evaporation of water and melting of the gel.[48] The second 4.1% weight loss appeared at temperatures from 210 to 300 °C, which is attributed to the continued removal of residues in the gel structure. The third step is apparent at temperatures from 300 to 500 °C with a prominent exothermic peak at 418.4 °C, corresponding to 30% weight loss. This weight loss is attributable to the dehydration and combustion of nitrate precursors to form chemical bonds in the gel. The last very weak and broad peak is observed in the range of 500−600 °C with small temperature peak at 547.1 °C, which was assigned to the formation of ilmenite CoTiO$_3$.[49] The results of the TGA−differential scanning calorimetry (DSC) analysis show that the total mass loss in the whole process is 62.5% and the weight loss ends at around 600 °C or more. Based on the TGA analysis, to obtain CoTiO$_3$ powder, the as-prepared CoTiO$_3$ gel should be calcined at a temperature of 600 °C or higher.

The influence of the calcining mode and the CTO composition in the mixed catalysts on the materials' physicochemical properties was studied to determine the appropriate synthesis procedure. The XRD patterns of CoTiO$_3$ calcined at 600−750 °C and for various durations are shown in Figure 2. The characteristic XRD peaks at 2θ = 23.8, 32.6, 35.2, 40.2, 48.7, 53.1, 61.2, and 63.1° with the strongest intensity at 2θ = 32.6°, which could be attributed to the (012), (104), (110), (113), (024), (116), (214), and (300) reflections for ilmenite CoTiO$_3$ (JCPDS card no. 15−0866), are observed in each samples. Notably, there is a little rutile phase TiO$_2$ (2θ = 27.5°) and cobalt oxide Co$_3$O$_4$ (2θ = 31.0, 36.6, 38.3, 44.5, 55.2, 58.9, and 64.7°) found as an impurity in the sample after calcination at 600 and 750 °C. However, pure ilmenite CoTiO$_3$ is obtained after calcination at 650 or 700 °C. No characteristic peaks of TiO$_2$ and Co$_3$O$_4$ impurities indicate that the products are pure CoTiO$_3$ in CTO-650 and CTO-700 samples. Among the samples, CTO-650 has the strongest intensity of perovskite CoTiO$_3$ characteristic peaks, indicating that this sample has the best crystallinity. Similarly, the suitable calcination time was selected as 2 h, since the XRD pattern of the CTO-2h sample showed no characteristic peaks of TiO$_2$ and Co$_3$O$_4$ impurities and pure ilmenite CoTiO$_3$ appeared with the highest crystallinity. Meanwhile, in the XRD spectrum of samples calcined at 1 or 3 h, the characteristic peaks for rutile TiO$_2$ and Co$_3$O$_4$ appear apparently in addition to the CoTiO$_3$ crystal signals. Therefore, the most favorable calcination mode is 650 °C and 2 h, and the CTO-650-2h sample was used in the synthesis of composite material and was labeled CTO/Ti.
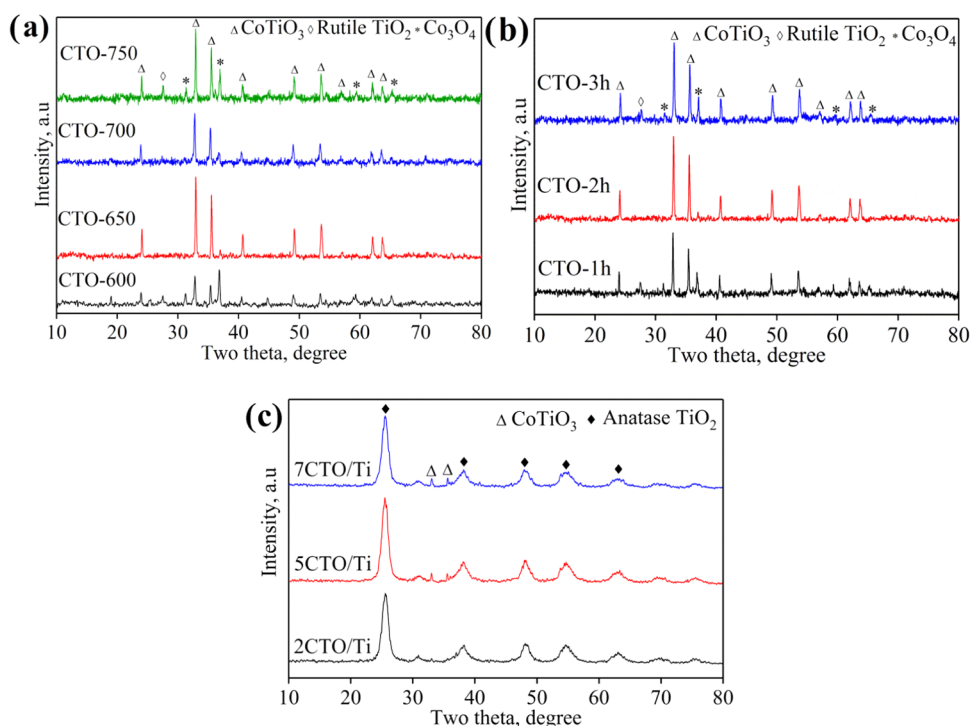
Figure 2. XRD patterns of the $CoTiO_3$ perovskite calcined at various temperatures for 2 h (a), at 650 °C for various durations (b), and CTO/Ti catalysts (c).

Table 1. Crystalline Size of the TiO_2 Anatase at $2\theta = 25.7°$ (d_{Ti}) and $CoTiO_3$ at $2\theta = 32.6°$ (d_{CTO}) from the XRD Pattern, the Specific Surface Area (S_{BET}), the Pore Volume (V_{pore}), and the Pore Size (d_{pore}) from BET Adsorption Isotherms, the Band Gap Energy (E_g), and the Absorbable Wavelength (λ) of the Synthesized Catalysts

catalyst	d_{Ti}, nm	d_{CTO}, nm	S_{BET}, m²/g	V_{pore}, cm³/g	d_{pore}, nm	E_g, eV	λ, nm
Ti-w	7.1		84.8	0.100	2.20	3.14	395
CTO		39.9	8.5	0.005	1.80	2.26	549
5CTO/Ti	7.9	30.9	130.5	0.171	2.44	3.09	402
7CTO/Ti	8.5	31.5	120.7	0.078	2.44	3.08	403

As shown in Figure 2c, XRD patterns of the mixed CTO/Ti catalysts showed diffraction peaks at 2θ of 33.0 and 35.6°, confirming the formation of $CoTiO_3$ (JCPDS card no. 15−0866). Simultaneously, the diffraction peaks at 2θ values of 25.7, 38.2, 48.1, 54.6, and 63.1° could also be assigned to anatase TiO_2 (JCPDS card no. 21−1272). As for the composites, the intensities of the main diffraction peaks for perovskite CTO increase with increasing content of CTO, suggesting the coexistence of both CTO and anatase TiO_2 crystals on a heterostructure catalyst. No other new crystalline phases have been found in all mixed catalysts, suggesting high purity of the composite samples. Especially, for the 2CTO-Ti sample, due to the low CTO content (2%), the characteristic peaks of $CoTiO_3$ were almost not observed.

Based on the XRD results at $2\theta = 32.6°$ of the (104) $CoTiO_3$ perovskite and at $2\theta = 25.7°$ of the TiO_2 anatase phase, their average crystal size is calculated by the Debye−Scherrer equation[50] and shown in Table 1. It has been found from Table 1 that the average crystal sizes of TiO_2 anatase and $CoTiO_3$ are in the range of 7.1−8.5 and 30.9−39.9 nm, respectively. In the mixed samples, the crystal size of TiO_2 anatase increased slightly, while that of CTO decreased. Of the mixed samples, a sample containing 5%CTO possessed the smallest crystalline size of CTO and TiO_2, being 30.9 and 7.9 nm, respectively.

In the Raman spectra in Figure 3a characteristic shifts at 195, 233, 264, 335, 383, 478, 520, 608, and 689 cm⁻¹ are observed, confirming that the CTO-650-2h sample is $CoTiO_3$. The Raman shift at 689 cm⁻¹ is ascribed to the symmetric vibrational mode of the CoO_6 octahedron (regular CoO_6 octahedron A_{1g} symmetry).[51] In the Raman spectra of the mixed samples (Figure 3b), the strong peak at 147 cm⁻¹, assigned to the strongest mode of anatase TiO_2, shows the presence of anatase TiO_2 on the CTO/Ti catalysts. In addition, four weak modes from anatase TiO_2 were expected at 199, 402, 517, and 641 cm⁻¹. Among characteristic modes of anatase TiO_2, A_{1g} (517 cm⁻¹)/B_{1g} (402 cm⁻¹) were related to antisymmetric/symmetric bending vibrations of O−Ti−O; while E_g at 147, 199, and 641 cm⁻¹ was associated with O−Ti−O symmetric stretching vibrations.[52] There is almost no appearance of characteristic peaks of $CoTiO_3$ due to its low content.

The chemical structure and functional groups of the as-synthesized samples were further studied by FT-IR spectra, which are illustrated in Figure 3c. In all samples, including pure CTO, Ti-w, and mixed samples, the peaks at 3435 and 1635 cm⁻¹ corresponding to the O−H stretching of the physically absorbed H_2O on the surface of catalysts and O−H bending vibration of water molecules, respectively,[53] as well as the vibration of C−H bonds of organic compounds at wavelengths
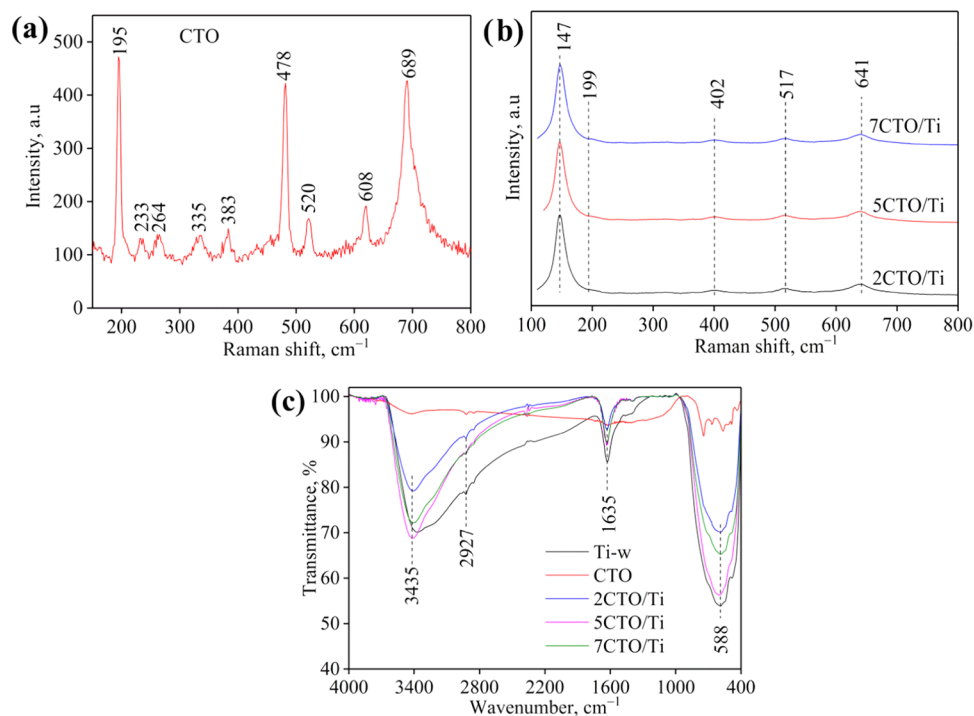
Figure 3. Raman spectra of the synthesized CTO-650-2h (a) and CTO/Ti (b), and FT-IR spectra (c) of CTO/Ti catalysts.
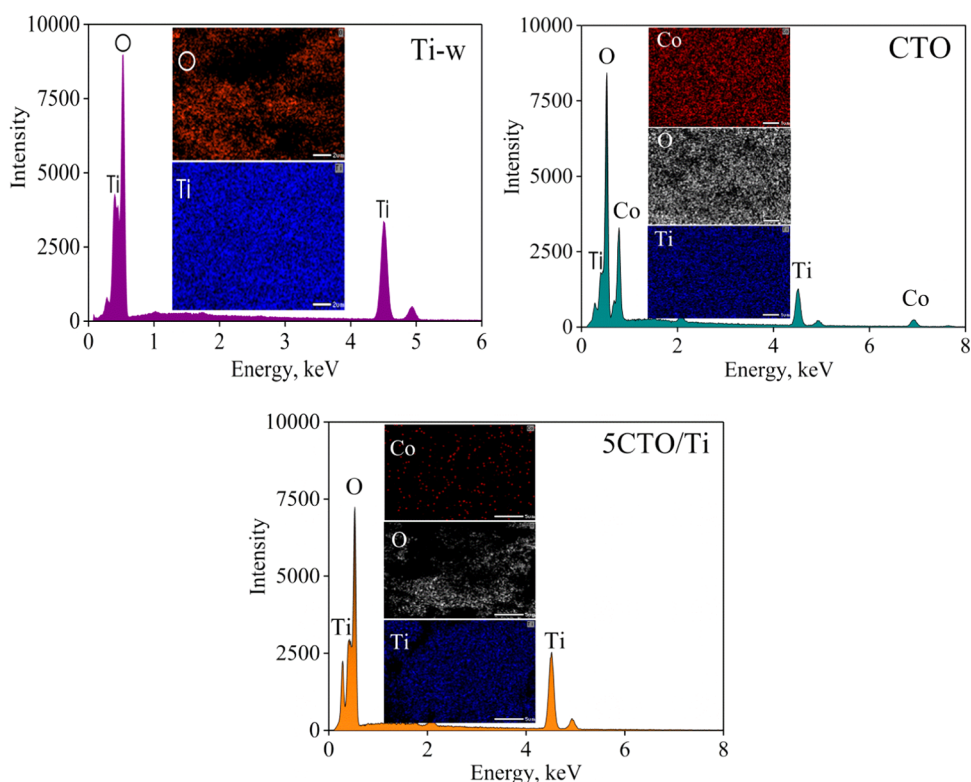

Figure 4. EDS mapping and EDX spectrum of the synthesized Ti-w, CTO, and 5CTO/Ti catalysts.

of 2930−2850 cm^{-1}, were apparently visible.[54] The strong bands at around 400−800 cm^{-1}, which are attributed to the Ti−O and Ti−O−Ti stretching vibrations,[55] and the band at 588 cm^{-1} attributed to the vibration of Ti−O[56] also appeared on the FT-IR spectrum of all samples. In the case of pure CoTiO$_3$, in addition to the above bands, the band appearing at 1090 cm^{-1} was associated with the Co−O group linked to Ti,

which reveals the formation of CoTiO$_3$.[55] The presence of hydroxyl groups on the surface of the catalyst was considered a vital factor for enhancing photocatalytic activity. Notably, the intensity of the hydroxyl groups on the mixed samples was significantly stronger than that of the CTO, but comparable to the Ti-w sample. Of the mixed samples, 5CTO/Ti is the

sample with the strongest intensity of −OH groups, which is expected to possess outstanding photocatalytic activity.

The elemental distribution and composition of the catalysts including Ti-w, CTO, and 5CTO/Ti were analyzed by energy-dispersive X-ray spectroscopy (EDX). The EDX images of the samples (Figure 4) reflect the presence of Co, Ti, and O elements, where the distribution of Co and Ti elements is entirely even on the surface of CTO-containing samples. On the EDX spectrum, the peaks at 0.4, 4.5, and 4.9 keV were assigned to the Ti element, while peaks at 0.8 and 6.9 keV were linked to the binding energies of Co, and the O signal appeared at 0.5 keV, which can be seen. From Table 2, the weight

Table 2. Elemental Composition from the EDX Spectrum

catalyst	weight from experiment, %			weight from calculation, %		
	Co	Ti	O	Co	Ti	O
Ti-w	0	59.4	40.6	0	60.0	40.0
CTO	39.6	28.3	32.1	38.1	31.0	30.9
5CTO/Ti	0.5	57.5	42.0	3.5	57.3	39.2

composition of the elements determined based on the EDX spectrum of the individual Ti-w and CTO samples was relatively consistent with the ideal data. For the 5CTO/Ti heterostructure sample, the experimental composition of Co is lower, and the O is higher than the theoretical value, that is, $CoTiO_3$ is distributed both on the surface and inside the mixed catalyst bulks.

FE-SEM and TEM technologies were used to investigate the surface morphology of catalysts. As observed from the FE-SEM image (Figure 5), the CTO sample is characterized by large particles (30−60 nm in size) and the particles agglomerated together to form larger bulks with a smooth surface. Meanwhile, on CTO and CTO/Ti samples the SEM (Figure 5) and TEM images (Figure 6a) showed a quasi-sphere-like morphology with a diameter of 5−7 nm.

After introducing $CoTiO_3$, the $CoTiO_3$ crystals, shown as dark particles in the HR-TEM images of 5CTO/Ti (Figure 6a), were found anchored on the surface of TiO_2 anatase particles and even inserted into the TiO_2 volume, which was confirmed by the elemental composition analysis by EDX (Table 2), as the weight content of Co from the experiment is much lower than the theoretically predicted results (0.5 vs 3.5%). As shown in the HR-TEM image (Figure 6b), the $CoTiO_3$ crystal and TiO_2 anatase combine closely with each other to form a smooth interface along their boundaries. The formed intimate interfaces in the heterostructured $CoTiO_3$/TiO_2 facilitate the migration of photogenerated charge carriers, limiting the recombination of photogenerated electron−hole pairs that enhance the photocatalytic activity.

Thus, in this study by the green hydrothermal method, the heterostructured CTO/Ti has been synthesized with uniform and separate particles evenly distributed, as seen in Figure 6a. The TiO_2 particle size estimated from the TEM image (Figure 6a), distributed in a narrow range, 5−7 nm, while the CTO particles, shown in Figure 6b, are about 2−3 nm. In addition, there were more porous channels of anatase TiO_2 comprised of the 5CTO/Ti catalyst. From the higher resolution image (Figure 6b), lattice fringe spacing was 0.38 nm. This results in a much larger surface area of the heterostructured samples than
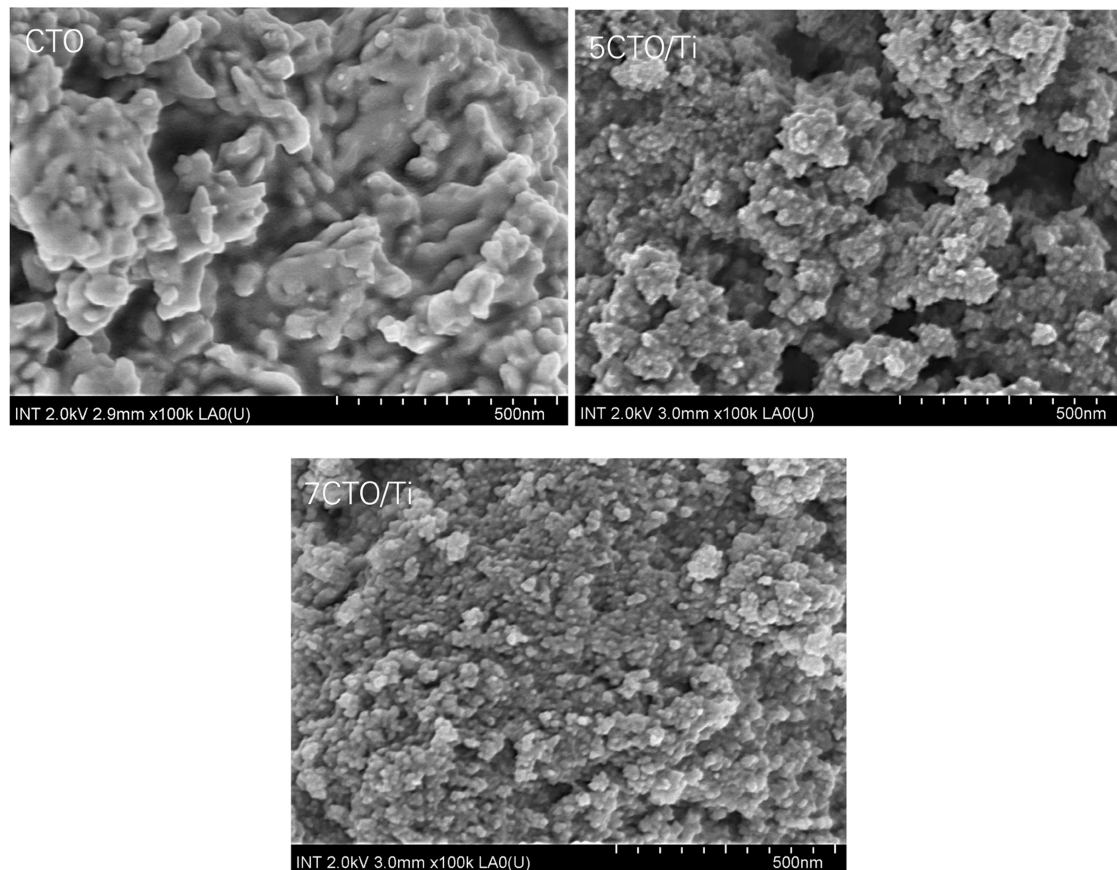

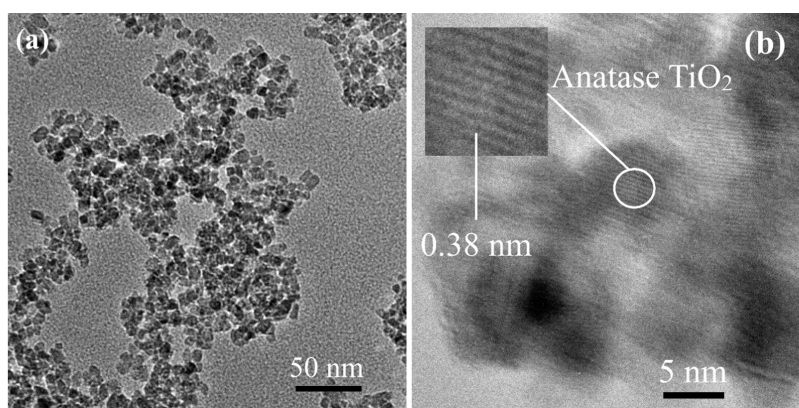**Figure 5.** FE-SEM images of the synthesized CTO, 5CTO/Ti, and 7CTO/Ti catalysts.

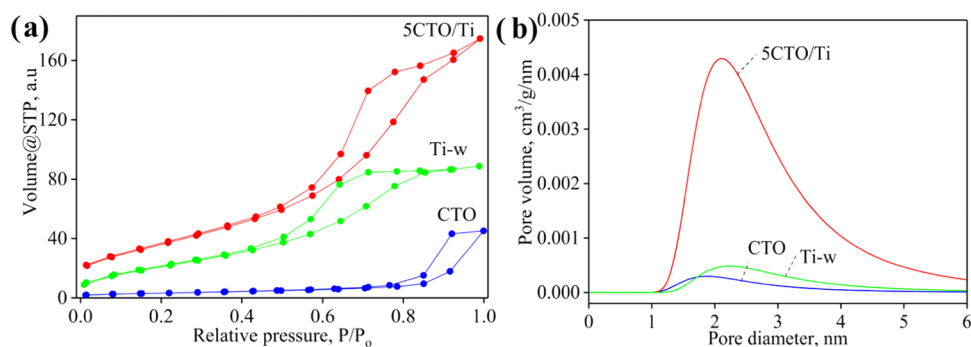**Figure 6.** High-resolution transmission electron microscopy (HR-TEM) images of the 5CTO/Ti catalyst.

Figure 7. N$_2$ adsorption/desorption isotherms (a) and the pore size distribution (b) of the synthesized Ti-w,[60] CTO, and 5CTO/Ti catalysts.
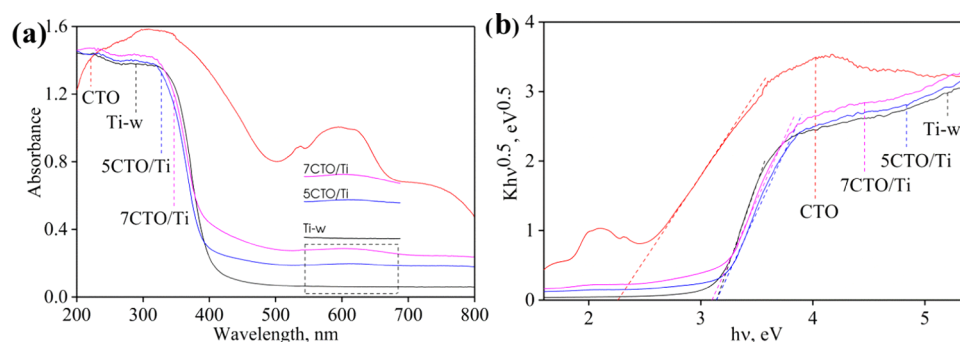

Figure 8. UV−vis diffuse reflectance spectra (a) and Tauc plot (b) of the synthesized catalysts.

that of the CTO (130 vs 8.5 m^2/g), as shown in Table 1. Notably, the particle sizes of both TiO$_2$ and CoTiO$_3$ in the mixed sample were smaller than the average crystallite size, determined from XRD patterns. This is explained by the close interlacing and interaction between TiO$_2$ and CTO, leading to the splitting of their crystals. From the above results, it is confirmed that the CoTiO$_3$/TiO$_2$ heterojunction structures have been constructed.

The pores are studied using N$_2$ adsorption−desorption isotherms shown in Figure 7. The common characteristics of the N$_2$ adsorption/desorption isotherms of Ti-w, CTO, and 5CTO-Ti samples (Figure 7) are that there is no inflection point, the adsorption and desorption branches coincide at relative pressure P/P_o below a certain value, and then, when P/P_0 is higher than this value the adsorption and desorption curves separate, and the adsorption hysteresis loop appears, which is consistent with the IV(a) type curve.[57] This means mesopores are present in the material structure and the

capillary condensation phenomenon occurs. The shape of the adsorption/desorption isotherm of the Ti-w, CTO, and 5CTO-Ti samples correspond to the H1−H2 hysteresis rings.[57] A hysteresis loop without the inflection point belongs to type H1 of Ti-w and CTO samples correspond to cylindrical pores with openings at both ends.[57] The hysteresis loop type H2(b) of the CTO/Ti mixed sample exhibits more complex pore structures and more random distribution of pores and an interconnected pore system in the heterostructure sample[57] that affects the textural properties of the CTO/Ti catalysts, such as surface area, pore volume, and pore size. Indeed, among the catalysts investigated, CTO/Ti has the steepest isotherm slopes and the most significant deviation between the adsorption and desorption branches, thus having the largest pore size (2.44 nm), pore volume (0.171 cm^3/g), and specific surface area (130.5 m^2/g) (Table 1). Specifically, the surface area of the 5CTO/Ti heterostructure was 1.5 times higher than that of the Ti-w catalyst. The existence of open cylindrical

pores with a larger diameter of the heterostructured CTO-Ti sample provides superior adsorption capacity compared to other catalysts.

Furthermore, in the first stage of the isotherms, for the CTO sample the adsorption quantity increases very gradually with the increase of the relative pressure, which suggests the presence of micropores (<2 nm).[58] In fact, the pore diameter of CTO was determined to be 1.8 nm. The steeper isotherm slopes of Ti-w and CTO-Ti samples indicate the higher average pore radius, being 2.2 and 2.44 nm respectively. This shows that the introduction of CTO to TiO_2 has significantly improved the surface feature through the formation of the CTO/Ti heterojunction structures, although CTO has a very low specific surface area (8.5 m^2/g) and pore volume (0.005 cm^3/g). The superior specific surface area of the composite samples may result from their heterojunction structures leading to the creation of many small, separate particles, and the intergranular slits form the secondary surface. The porous structure increases the surface area and thus offers more active sites.[59]

As seen from the absorption spectra in Figure 8, $CoTiO_3$ absorbs light in two regions. The first UV region is below 500 nm due to $O^{2-} \rightarrow Ti^{4+}$ charge transfer.[48] The second visible region is in the range of 500−670 nm, centering at ca. 574 nm, due to d−d transition of Co^{2+} ions.[61] The band gap (E_g) of the obtained $CoTiO_3$ perovskite is calculated to be approximately 2.26 eV based on the Tauc plot (Figure 8b), which is approximate to previous studies (2.25 eV^{62} and 2.28 eV^{48}). Pure Ti-w has an absorption onset at 395 nm, corresponding to the band gap energy of 3.14 eV.[60] When $CoTiO_3$ is added into Ti-w, a weak additional visible-light absorption range (500−670 nm), which is a characteristic of $CoTiO_3$, can be found in the composite. On increasing the loading amount of $CoTiO_3$ to 7 wt%, the intensity of the visible absorption peak increases. As shown in Figure 8b, the band gap energies of 5CTO/Ti and 7CTO/Ti catalysts were 3.09 and 3.08 eV, respectively. The extension of adsorption to the visible-light region may be beneficial for enhanced photoactivity of the heterostructured catalyst.[63] With this band gap value, UVA light is suitable for catalyst activation.

Photocatalytic Activity of the Obtained Materials. The experimental result showed that the adsorption/desorption equilibrium of cinnamic acid on the catalysts reached after 40 min and the amount of CA adsorbed on the catalyst surface in the dark and decomposed by UVA light (without catalyst) on all catalysts is negligible. Then, before starting the reaction, the catalyst-containing solution was stirred in the dark for 40 min to establish the adsorption/desorption equilibrium.

Comparison of the activity of the studied catalysts. The photocatalytic activity of Ti-w, CTO, and CTO/Ti hetero-structures for the degradation of CA was investigated. An obvious degradation of CA was observed under UVA light in the presence of the synthesized catalysts. The efficiency of CA removal after 90 min was 75.2, 79.7, 80.9, and 66.5% for Ti-w, 2CTO/Ti, 5CTO/Ti, and 7CTO/Ti, respectively (Figure 9). Compared with Ti-w, $CoTiO_3$ exhibits much lower activity under the same experimental conditions (X_{90} = 4.6 vs 67.1%), implying that $CoTiO_3$ is the less active component for CA photodegradation. The low photoactivity of pure $CoTiO_3$ is caused by the high recombination rate of photogenerated electron−hole pairs[64] and low specific surface area. The results in Figure 9 indicate that although pure $CoTiO_3$ does not show
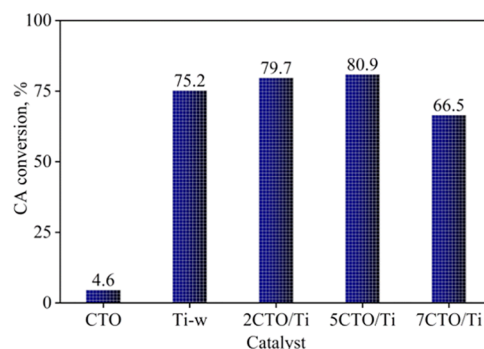
Figure 9. CA removal efficiency for 90 min (X_{90}) in photocatalytic reaction on the synthesized Ti-w, 2CTO/Ti, 5CTO/Ti, and 7CTO/Ti catalysts at pH = 3.8, C_{cat} = 0.75 g/L, Q_{air} = 0.3 L/min, and T = 25 °C.

a satisfactory CA degradation activity, the mixed sample CTO/Ti was demonstrated to be a highly photo-oxidizing catalyst under UVA light. As the content of CTO increased, the photocatalytic activity increased at first but decreased when the value of CTO reached 7%. The lower activity of the 7CTO/Ti sample compared to that of the 5CTO/Ti sample due to a decline in the surface with high content of the perovskite,[22] larger crystal size of TiO_2 and $CoTiO_3$, and lower density of hydroxyl groups on the surface. Specifically, with increasing CTO content from 5 to 7% the specific surface area reduces from 130.5 to 120.7 m^2/g. The large surface area was an important factor in improving the photocatalytic performance of the 5CTO/Ti heterostructured sample based on active sites present on the catalyst surface. The observed decrease in photocatalytic efficiency of CTO/Ti with a high $CoTiO_3$ content (7%) could also be caused by the agglomeration of $CoTiO_3$ crystals, as seen in the FE-SEM image, and act as the recombination centers of photogenerated charge carriers and destroy the formed heterojunction structures, thus inhibiting the transfer and separation of photogenerated electron−hole pairs.[65] The results show that controlling CTO content plays a decisive role in obtaining the highest activity in mixed CTO-Ti photocatalysts.

The CTO/Ti catalyst with 5% CTO provided the highest activity for CA degradation, with 90 min CA conversion reaching 80.9%, much higher than that of pure $CoTiO_3$ (4.6%) and even higher than Ti-w (75.2%). The high activity of the 5CTO/Ti catalyst is most likely related to its heterojunction structures, which provide a high specific surface area, and more hydroxyl groups on the surface of the catalyst, consequentially supplying greater amounts of active species.

It was reported by Wangkawong et al.[63] that when methylene blue (MB) photodegradation was performed under an O_2 atmosphere the performance reached 12.2%, while it almost stopped when the reaction was performed under a N_2 atmosphere. According to the authors, it is likely that e−h[+] recombination in the $CoTiO_3$ system highly competes with the photocatalytic reaction, thus resulting in very low generations of $^{\bullet}OH$ and $^{\bullet}O_2^{-}$. Additionally, the results confirm the important role of dissolved oxygen in scavenging the conduction band electrons and,supporting the hypothesis that the photogenerated charge recombination occurs in the $CoTiO_3$ system.

In our study, for the 5CTO/Ti heterostructure system Figure 10b shows that the reduction in airflow rate does not apparently decrease the photocatalytic performance of the
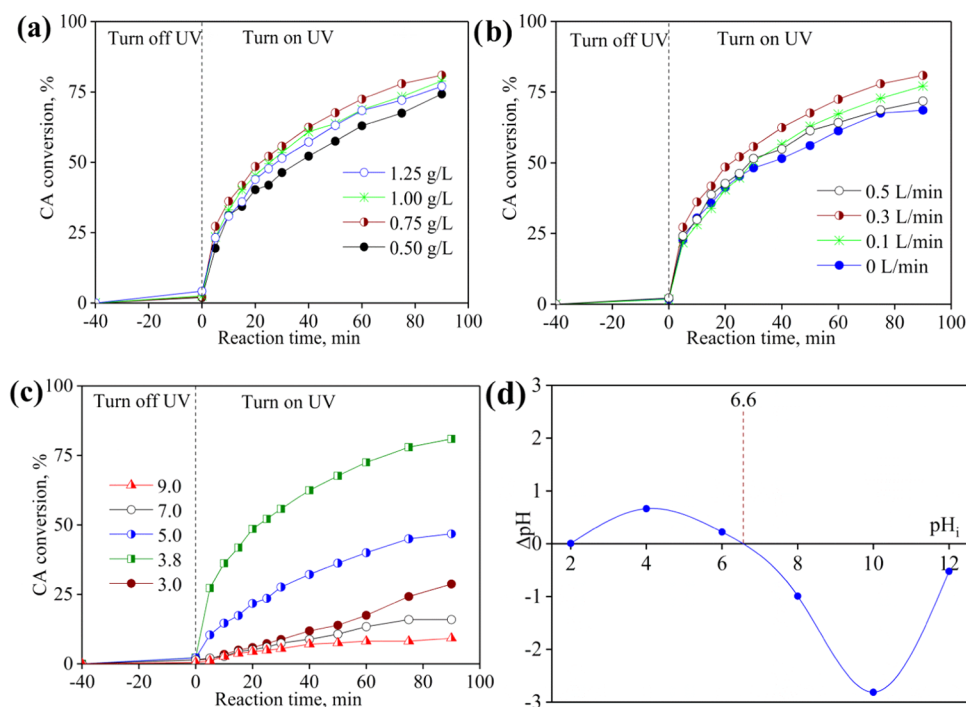
Figure 10. Effects of the conditions for the photocatalytic degradation of cinnamic acid at $T = 25$ °C: (a) Influence of the catalyst dosage (pH = 3.8, Q_{air} = 0.3 L/min), (b) the airflow rate (pH = 3.8, C_{cat} = 0.75 g/L); (c) the initial pH of solution (C_{cat} = 0.75 g/L, Q_{air} = 0.3 L/min), and (d) PZC of the 5CTO/Ti nanocatalyst.

material. Specifically, reducing the airflow from 0.5 to 0 L/min led to a maximum decrease in 90 min CA conversion of 12%, from 80.9 to 68.6%. Especially, when the reaction was performed under a N_2 atmosphere the CA conversion remained high (X_{90} = 68.6%). Under the same conditions when the pure CTO catalyst was used the CA conversion was very low, and the CA degradation stopped when the reaction was carried out under a N_2 atmosphere. This result shows that compared with pure CTO, the CTO-Ti catalyst exhibits a high generation of active species as a result of improved light absorption and an efficient e−h$^+$ separation upon the heterojunction formation between $CoTiO_3$ and Ti-w, enhancing the physicochemical properties.[15]

$CoTiO_3$ in the hybrid catalyst probably plays two important roles: one is enhancing the visible-light-absorption ability of the composite; another is increasing the e−h$^+$ separation efficiency induced by the hybridization effect between TiO_2 and $CoTiO_3$. Upon coupling TiO_2 with $CoTiO_3$, an efficient e−h$^+$ charge transfer between the two materials and an enhanced visible-light-absorption ability were achieved. Under visible-light irradiation, $CoTiO_3$ can be activated to generate e−h$^+$ pairs that act as photosensitizers and transferred their electron to the conduction band of TiO_2. Because the electrons in the conduction band of TiO_2 is less negative (−0.29 eV) than the potential of $O^2/O_2^{\bullet-}$ (−0.33 eV), they could reduce O_2 to $O_2^{\bullet-}$ superoxide. The superoxide radicals could react with adsorbed H_2O molecules on the surface of the catalyst or the H$^+$ ions present in the solution to form $^{\bullet}OH$ radicals. The holes (h$^+$) in the valance band of CTO/Ti react with OH− on the catalyst surface to form $^{\bullet}OH$ radicals because the holes in the valence band of CTO (2.66 eV) and TiO_2 (2.91 eV) are more positive than $^{\bullet}OH/OH^-$ (1.99 eV). XRD patterns and the Raman spectra of the mixed CTO/Ti catalysts confirmed the formation of $CoTiO_3$ and anatase TiO_2 and their close

combination forms a smooth interface along the boundaries, which facilitates the migration of photogenerated charge carriers, limiting the recombination of photogenerated electron−hole pairs. Moreover, the number of the hydroxyl groups on the mixed samples was significantly increased as compared to the CTO and comparable to the Ti-w sample. All these factors enhance the photocatalytic activity.

Effects of the Reaction Conditions. The actual efficiency of the catalyst is determined by internal factors (composition and properties of the catalyst) and extrinsic factors (reaction conditions). The influence of reaction conditions on CA decomposition efficiency was investigated to select the most favorable reaction conditions and is reflected in Figure 10.

The influence of photocatalyst dosages on photocatalytic activity for CA degradation is illustrated in Figure 10a. First, CA conversion increased with increasing catalyst dosage (C_{cat}) from 0.5 to 0.75 g/L, changed insignificantly with a further increase in catalyst dose to 1.0 mg/L, and then decreased when the catalyst dose increased to 1.25 g/L. Commonly, the conversion increases as the catalyst content increase due to the increase in the number of active sites. However, in the photocatalytic reaction, when the increase in the catalyst concentration was excessively high (above 1 g/L), a decrease in conversion with increasing catalyst content was observed. This is due to the aggregation of the photocatalyst and interception of light occurring at a higher dosage of 1.25 g/L.[66]

The effect of the airflow rate on CA degradation efficiency is shown in Figure 10b. During the photocatalytic reaction, airflow functioned as a promoter by introducing molecular oxygen. Oxygen molecules in the airflow reacted with the free electrons, formed at the active sites on the catalyst surface and prevented the recombination of the electron−hole pairs. As a result, more oxidative radicals were generated to oxidize organic pollutants.[67] CA degradation was favored by a high
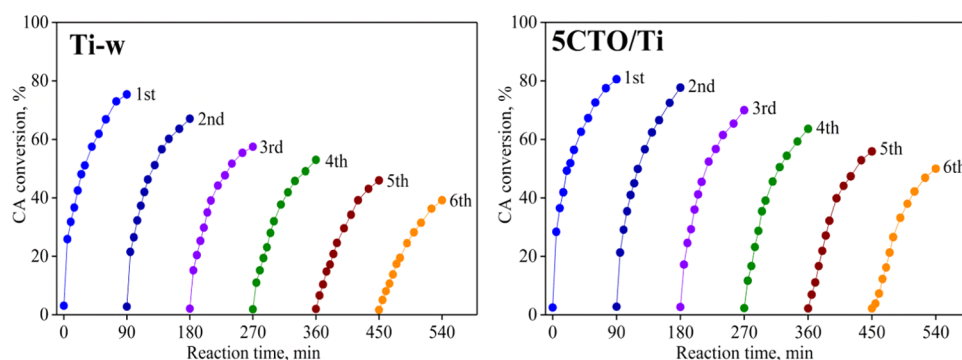
Figure 11. The recyclability of the Ti-w and 5CTO/Ti catalysts for CA degradation at pH = 3.8, C_{cat} = 0.75 g/L, Q_{air} = 0.3 L/min, and T = 25 °C.

airflow rate of 0.3 L/min, mainly due to the increase in active species. At lower airflow of 0.1 L/min or the absence of oxygen, there was a lower efficiency for CA degradation compared to the introduction at 0.3 L/min due to a deficiency of active species. Conversely, the light absorbance on the catalyst surface was hindered at a high concentration of oxygen[68] leading to a decrease in CA conversion at an airflow rate of 0.5 L/min. Additionally, a decline in CA degradation at the high oxygen concentration is also due to the nonselective oxidation of the oxidative radicals.[69]

Figure 10c shows the dependence of CA degradation on the initial pH of CA solution. The optimal pH for CA conversion was recognized to be 3.8. The isoelectric point of 5CTO/Ti was determined to be 6.6 (Figure 10d). Electrostatic attraction promoted CA adsorption because the surface 5CTO/Ti was positively charged at pH = 3.0, 3.8, and 5.0. In contrast, negative charges were formed on the catalyst surface at pH = 7.0 and 9.0. As a result, electrostatic repulsion was dominant between deprotonated CA (pK_a = 4.44) and the catalyst surface leading to minimization of CA adsorption.[70] At pH = 3.0, CA mainly existed in neutral molecules,[71] reducing CA adsorption. Furthermore, the pH of the solution also affected the formation of active species. Normally, the degradation of contaminants decreased in a strong base and strong acid, which are unfavorable for forming hydroxyl radicals. In contrast, the weakly acidic to neutral environment favored the formation of hydroxyl radicals.[72] The degradation efficiencies were recorded 28.7, 80.9, 46.8, 15.9, and 9.2% after 90 min of reaction with pH values of 3.0, 3.8, 5.0, 7.0, and 9.0, respectively.

From the obtained results, the optimal conditions for CA photodegradation were found as follows: the catalyst dosage of 0.75 g/L, the airflow rate of 0.3 L/min and the initial pH of the solution of 3.8. The recycling experiment for CA photodegradation was conducted under these most favorable conditions.

The recyclability of photocatalysts is crucial for practical applications in photocatalysis. The recycling of the 5CTO/Ti catalyst was experimentally investigated for CA degradation to compare with the Ti-w catalyst, and the results are shown in Figure 11. After six consecutive cycles, the 90 min CA conversion of the 5CTO/Ti catalyst reduced approximately by 38.0 from 80.9% in the first cycle to 50.0% in the sixth cycle, while on the Ti-w catalyst X_{90} decreased by 48% after 6 cycles, from 75.2 to 39.2% under the same reaction conditions. This indicates that the 5CTO/Ti heterostructured material had better stability than Ti-w for CA removal. The reduction in CA conversion of the catalyst was due to the covering of the active

sites on the surface by the degraded sediments and loss of catalyst for CA elimination from the reaction mixture.[69]

Recently, $CoTiO_3$ has received enormous attention in the field of photocatalysis because of its narrow band gap, suitable electronic band structure, strong visible-light absorption, and high stability.[15] Many attempts have been made to improve the photocatalytic activity of $CoTiO_3$. Currently, the research on the synthesis and application of perovskite $MTiO_3$-TiO_2 heterostructure catalysts in general and $CoTiO_3$-TiO_2 is still limited. Especially, their application in the photocatalytic degradation of polluted phenolic compounds such as cinnamic acid rarely appear in publications.

To date, very few publications allow a comparison of the activity of CTO-TiO_2 in the photodegradation of a representative phenolic compound, cinnamic acid. It was reported[23] that the combination of $NiTiO_3$ with TiO_2 enables a red-shift in the absorption band from UV (λ = 385 nm) to UV-A light (λ = 404−412 nm). The 1.0 wt % $NiTiO_3$ in $NiTiO_3$/TiO_2 composite was found to maximize CA photodegradation with 90 min conversion, reaching 73.7%. Compared with the 5CTO-Ti catalyst 1%$NiTiO_3$−TiO_2 (NTO/Ti) was found to have lower activity under the same reaction conditions despite its better physicochemical properties. The $NiTiO_3$/TiO_2 catalyst possessed a higher specific surface area (145.4 m^2/g) and pore volume (0.182 cm^3/g), and lower band gap energy (3.02 eV) compared with CTO-Ti. Notably, the typical characteristics of $CoTiO_3$ and $NiTiO_3$ perovskites possess low band gap energy (~2.2 eV) and low catalytic activity of CA photodegradation under UVA light (X_{90} = 4.6 and 3.8% respectively). The reason for the low photocatalytic activity of $NiTiO_3$ is that the crystal structure of $NiTiO_3$ consists of alternating NiO_6 and TiO_6 layers and induces a wide energy gap from the hybridized Ni 3d and O 2p orbitals to the predominant Ti 3d orbitals, blocking both Ni^{2+} → Ti^{4+} and O 2p → Ti 3d charge-transfer transitions.[64] When $NiTiO_3$ was incorporated into TiO_2 the change in the phase composition of TiO_2 from pure anatase (E_g = 3.2 eV) to a mixture of anatase (E_g = 3.2 eV), rutile (E_g = 3.1 eV), and brookite (E_g = 1.86 eV) crystalline phases and the occurrence of O^{2-} → Ti^{4+} charge-transfer band of $NiTiO_3$ caused a decrease in the band gap energy.[73] The mixed catalyst $NiTiO_3$-TiO_2 showed a much higher degradation rate of cinnamic acid than pure $NiTiO_3$. However, with a low $NiTiO_3$ optimal load (1%), the activity improvement of the TiO_2-based catalyst was not obvious, although the specific surface area and porosity of the catalyst were improved. Meanwhile, the CTO/Ti composite system in this study exhibited an improved activity comparison with TiO_2 and the reason for this enhancement

was explained to be related to the formation of a heterojunction structure. Two causes of low photocatalytic activity of $CoTiO_3$, i.e., high recombination of the photogenerated $e−h^+$ pair and low specific surface area of the perovskite, have been demonstrated to be overcome in the mixed catalyst.

In addition to combining with the TiO_2 photocatalyst, in some studies, CTO is also mixed with other semiconductors to overcome its disadvantages and construct more efficient photocatalysts. Coupling $CoTiO_3$ with other semiconductors with suitable band edges to create the composite photocatalysts, such as $CoTiO_3/Ag_3VO_4$ causes an efficient charge separatation and improved photocatalytic performance for the photocatalytic degradation of methylene blue.[63] In the $CoTiO_3/Ag_3VO_4$ composite the heterostructure was formed. The $CoTiO_3/gC_3N_4$ heterostructures obtained by the combination of visible-light sensitizer $CoTiO_3$ (E_g = 2.33 eV) with a small band gap semiconductor g-C_3N_4 (E_g = 2.68 eV) exhibited remarkably improved photocatalytic performance for the degradation of methyl orange under visible-light irradiation in comparison with both pure g-C_3N_4 and $CoTiO_3$ thanks to the synergistic effect existing between g-C_3N_4 and $CoTiO_3$ and efficient spatial separation of photogenetrated electrons and holes on different sides of the heterojuction.[74]

The investigation results showed that mixing 5% CTO with TiO_2 increased the activity and durability of the titania catalyst thanks to the special heterojuction structure of the composite catalyst. This result shows that in addition to the traditional methods of doping TiO_2 with metals or nonmetals, it is possible to improve the performance of the traditional TiO_2 catalyst by combining it with a small band gap perovskite to construct a heterojunction-structure catalyst. A valuable feature of this investigation that should be noted is that the catalyst is synthesized by a green method, using water as the solvent.

CONCLUSIONS

The heterostructured $CoTiO_3/TiO_2$ catalysts have been successfully synthesized by a hydrothermal route in the water medium. The combination of $CoTiO_3$ with TiO_2 both overcomes the disadvantage of high recombination of the photogenerated $e−h^+$ pair and the low specific surface area of the $CoTiO_3$ perovskite and expands the light-absorption region of TiO_2, leading to increased activity in the photooxidation of cinnamic acid. The physicochemical properties and activity of the $CoTiO_3/TiO_2$ composite catalyst depend on the heat treatment regime and the $CoTiO_3$ content. Sample 5% $CoTiO_3/TiO_2$ calcined at 650 °C for 2 h had the highest purity and crystallinity. Excellent performance of the 5CTO/Ti catalyst was associated with the construction of a heterojunction structure that improves the specific surface area, porosity, and charge separation, enhancing the hydroxyl groups on the surface. The 5CTO/Ti catalyst exhibited better photocatalytic activity and stability than the Ti-w catalyst with the 90 min conversion of cinnamic acid reaching 80.9%, much higher than that of individual $CoTiO_3$ (4.6%) and TiO_2 (75.2%).

AUTHOR INFORMATION

Corresponding Author

Cam Anh Ha − *Ho Chi Minh City University of Technology (HCMUT), Ho Chi Minh City 700000, Vietnam; Vietnam National University Ho Chi Minh City, Ho Chi Minh City 700000, Vietnam;* orcid.org/0000-0001-7919-4028; Email: hcanh@hcmut.edu.vn

Authors

Dien Trung Nguyen − *Institute of Chemical Technology − Vietnam Academy of Science and Technology, Ho Chi Minh City 701000, Vietnam; School of Education, Can Tho University, Can Tho City 900000, Vietnam*

Tri Nguyen − *Institute of Chemical Technology − Vietnam Academy of Science and Technology, Ho Chi Minh City 701000, Vietnam; Ho Chi Minh City Open University, Ho Chi Minh City 700000, Vietnam;* orcid.org/0000-0001-9486-5096

Complete contact information is available at:
https://pubs.acs.org/10.1021/acsomega.2c04999

Notes

The authors declare no competing financial interest.

REFERENCES

(1) Krastanov, A.; Alexieva, Z.; Yemendzhiev, H. Microbial degradation of phenol and phenolic derivatives. *Eng. Life Sci.* **2013**, *13*, 76−87.

(2) Singh, T. S.; Mitra, S. Interaction of cinnamic acid derivatives with serum albumins: A fluorescence spectroscopic study. *Spectrochim. Acta, Part A* **2011**, *78*, 942−948.

(3) Mosse, K. P.; Verheyen, T. V.; Cruickshank, A. J.; Patti, A. F.; Cavagnaro, T. R. Soluble organic components of winery wastewater and implications for reuse. *Agric. Water Manage.* **2013**, *120*, 5−10.

(4) Yakhlef, W.; Arhab, R.; Romero, C.; Brenes, M.; de Castro, A.; Medina, E. Phenolic composition and antimicrobial activity of Algerian olive products and by-products. *LWT* **2018**, *93*, 323−328.

(5) Deeb, A. A.; Fayyad, M. K.; Alawi, M. A. Separation of polyphenols from Jordanian olive oil mill wastewater. *Chromatogr. Res. Int.* **2012**, *2012*, 1−8.

(6) Tang, C.; Liu, L.; Li, Y.; Bian, Z. Aerosol spray assisted assembly of TiO_2 mesocrystals into hierarchical hollow microspheres with enhanced photocatalytic performance. *Appl. Catal., B* **2017**, *201*, 41−47.

(7) Pare, B.; Jonnalagadda, S. B.; Tomar, H.; Singh, P.; Bhagwat, V. W. ZnO assisted photocatalytic degradation of acridine orange in aqueous solution using visible irradiation. *Desalination* **2008**, *232*, 80−90.

(8) Liu, X.; Zhu, G.; Wang, X.; Yuan, X.; Lin, T.; Huang, F. Progress in black titania: A new material for advanced photocatalysis. *Adv. Energy Mater.* **2016**, *6*, No. 1600452.

(9) Su, D.; Dou, S.; Wang, G. Anatase TiO_2: Better anode material than amorphous and rutile phases of TiO_2 for Na-ion batteries. *Chem. Mater.* **2015**, *27*, 6022−6029.

(10) Hu, Q.; Huang, J.; Li, G.; Jiang, Y.; Lan, H.; Guo, W.; Cao, Y. Origin of the improved photocatalytic activity of Cu incorporated TiO_2 for hydrogen generation from water. *Appl. Surf. Sci.* **2016**, *382*, 170−177.

(11) Raja, A.; Selvakumar, K.; Rajasekaran, P.; Arunpandian, M.; Ashokkumar, S.; Kaviyarasu, K.; Asath Bahadur, S.; Swaminathan, M. Visible active reduced graphene oxide loaded titania for photodecomposition of ciprofloxacin and its antibacterial activity. *Colloids Surf., A* **2019**, *564*, 23−30.

(12) Raja, A.; Rajasekaran, P.; Selvakumar, K.; Arivanandhan, M.; Asath Bahadur, S.; Swaminathan, M. Rational fabrication of needle with spherical shape ternary reduced Graphene Oxide-HoVO$_4$-TiO$_2$

photocatalyst for degradation of ibuprofen under visible light. *Appl. Surf. Sci.* **2020**, *513*, No. 145803.

(13) Qu, Y.; Zhou, W.; Ren, Z.; Du, S.; Meng, X.; Tian, G.; Pan, K.; Wang, G.; Fu, H. Facile preparation of porous $NiTiO_3$ nanorods with enhanced visible-light-driven photocatalytic performance. *J. Mater. Chem.* **2012**, *22*, 16471−16476.

(14) Raghavender, A. T.; Hoa Hong, N.; Joon Lee, K.; Jung, M. H.; Skoko, Z.; Vasilevskiy, M.; Cerqueira, M. F.; Samantilleke, A. P. Nano-ilmenite $FeTiO_3$: Synthesis and characterization. *J. Magn. Magn. Mater.* **2013**, *331*, 129−132.

(15) Wangkawong, K.; Tantraviwat, D.; Phanichphant, S.; Inceesungvorn, B. Band offsets of novel $CoTiO_3/Ag_3VO_4$ heterojunction measured by X-ray photoelectron spectroscopy. *Appl. Surf. Sci.* **2015**, *324*, 705−709.

(16) Boonprakob, N.; Wetchakun, N.; Phanichphant, S.; Waxler, D.; Sherrell, P.; Nattestad, A.; Chen, J.; Inceesungvorn, B. Enhanced visible-light photocatalytic activity of $g\text{-}C_3N_4/TiO_2$ films. *J. Colloid Interface Sci.* **2014**, *417*, 402−409.

(17) Su, X.; Fan, D.; Sun, H.; Yang, J.; Yu, Z.; Zhang, D.; Pu, X.; Li, H.; Cai, P. One-dimensional rod-shaped $Ag_2Mo_2O_7/BiOI$ n-n junctions for efficient photodegradation of tetracycline and rhodamine B under visible light. *J. Alloys Compd.* **2022**, *912*, No. 165184.

(18) Yao, X.; Zhen, H.; Zhang, D.; Liu, J.; Pu, X.; Cai, P. Microwave-assisted hydrothermal synthesis of broadband Yb^{3+}/Er^{3+} co-doped $BiOI/Bi_2O_4$ photocatalysts with synergistic effects of upconversion and direct Z-scheme heterojunction. *Colloids Surf., A* **2022**, *648*, No. 129276.

(19) Shao, Z.; Meng, X.; Lai, H.; Zhang, D.; Pu, X.; Su, C.; Li, H.; Ren, X.; Geng, Y. Coralline-like Ni_2P decorated novel tetrapod-bundle $Cd_{0.9}Zn_{0.1}S$ ZB/WZ homojunctions for highly efficient visible-light photocatalytic hydrogen evolution. *Chin. J. Catal.* **2021**, *42*, 439−449.

(20) Wu, F.; Yu, Y.; Yang, H.; German, L. N.; Li, Z.; Chen, J.; Yang, W.; Huang, L.; Shi, W.; Wang, L.; Wang, X. Simultaneous enhancement of charge separation and hole transportation in a $TiO_2\text{-}SrTiO_3$ core-shell nanowire photoelectrochemical system. *Adv. Mater.* **2017**, *29*, No. 1701432.

(21) Xing, C.; Liu, Y.; Zhang, Y.; Liu, J.; Zhang, T.; Tang, P.; Arbiol, J.; Soler, L.; Sivula, K.; Guijarro, N.; Wang, X.; Li, J.; Du, R.; Zuo, Y.; Cabot, A.; Llorca, J. Porous $NiTiO_3/TiO_2$ nanostructures for photocatalytic hydrogen evolution. *J. Mater. Chem. A* **2019**, *7*, 17053−17059.

(22) Huang, J.; Jiang, Y.; Li, G.; Xue, C.; Guo, W. Hetero-structural $NiTiO_3/TiO_2$ nanotubes for efficient photocatalytic hydrogen generation. *Renewable Energy* **2017**, *111*, 410−415.

(23) Nguyen, P. A.; Nguyen, T.; Ha, C. A.; Hoang, T. C.; Nguyen, T. T. V.; Nguyen, D. T.; Luu, C. L. Exceptional photodecomposition activity of heterostructure $NiTiO_3\text{-}TiO_2$ catalyst. *J. Sci.: Adv. Mater. Devices* **2022**, *7*, No. 100407.

(24) Lou, Z.; Li, Y.; Song, H.; Ye, Z.; Zhu, L. Fabrication of Fe_2TiO_5/TiO_2 nanoheterostructures with enhanced visible-light photocatalytic activity. *RSC Adv.* **2016**, *6*, 45343−45348.

(25) Phung Anh, N.; Tri, N.; Trung, N. D.; Anh, H. C.; Cuong, H. T.; Van, N. T. T.; Loc, L. C. Envirronmentally friendly fabrication of $Fe_2TiO_5\text{-}TiO_2$ nanocomposite for enhanced photodegradation of cinnamic acid solution. *Adv. Nat. Sci.: Nanosci. Nanotechnol.* **2022**, *12*, No. 045015.

(26) Trung, N. D.; Anh, H. C.; Tri, N.; Loc, L. C. Fabrication of TiO_2/Al_2TiO_5 nanocomposite photocatalysts. *Int. J. Nanotechnol.* **2020**, *17*, 607−622.

(27) da Silva, B. C.; Bastos, P. H. C.; Junior, R. B.; Checca, N.; Fréty, R.; Brandão, S. T. Perovskite-type catalysts based on nickel applied in the $Oxy\text{-}CO_2$ reforming of CH_4: Effect of catalyst nature and operative conditions. *Catal. Today* **2021**, *369*, 19−30.

(28) de Santana Santos, M.; Neto, R. C. R.; Noronha, F. B.; Bargiela, P.; da Rocha, M. d. G. C.; Resini, C.; Carbó-Argibay, E.; Fréty, R.; Brandão, S. T. Perovskite as catalyst precursors in the partial oxidation of methane: The effect of cobalt, nickel and pretreatment. *Catal. Today* **2018**, *299*, 229−241.

(29) Lima, S.; Assaf, J.; Peña, M.; Fierro, J. Structural features of $La_{1−x}Ce_xNiO_3$ mixed oxides and performance for the dry reforming of methane. *Appl. Catal., A* **2006**, *311*, 94−104.

(30) González-Varela, D.; Araiza, D. G.; Díaz, G.; Pfeiffer, H. $LaNiO_3$ perovskite synthesis through the EDTA−Citrate complexing method and its application to CO oxidation. *Catalysts* **2022**, *12*, 57.

(31) Zhang, Z.; Ou, Z.; Qin, C.; Ran, J.; Wu, C. Roles of alkali/alkaline earth metals in steam reforming of biomass tar for hydrogen production over perovskite supported Ni catalysts. *Fuel* **2019**, *257*, No. 116032.

(32) Ranganathan, R. V.; Jony, B.; Fondriest, S. M.; Liu, Z.; Wang, R.; Uddi, M. Plasma-catalysis chemical looping CH_4 reforming with water splitting using ceria supported Ni based La-perovskite nanocatalyst. *J. CO_2 Util.* **2019**, *32*, 11−20.

(33) Le, N. T. H.; Calderón-Moreno, J. M.; Popa, M.; Crespo, D.; Van Hong, L.; Phuc, N. X. $LaNiO_3$ nanopowder prepared by an 'amorphous citrate' route. *J. Eur. Ceram. Soc.* **2006**, *26*, 403−407.

(34) Yang, E.-H.; Kim, S. W.; Ahn, B. S.; Moon, D. J. Preparation and characterization of Ni-based perovskite catalyst for steam CO_2 reforming of methane. *J. Nanosci. Nanotechnol.* **2013**, *13*, 4334−4337.

(35) Wang, H.; Dong, X.; Zhao, T.; Yu, H.; Li, M. Dry reforming of methane over bimetallic Ni-Co catalyst prepared from La-$(Co_xNi_{1-x})_{0.5}Fe_{0.5}O_3$ perovskite precursor: Catalytic activity and coking resistance. *Appl. Catal., B* **2019**, *245*, 302−313.

(36) Ahmad, N.; Wahab, R.; Manoharadas, S.; Alrayes, B. F.; Alam, M.; Alharthi, F. A. The role of strontium in $CeNiO_3$ nano-crystalline perovskites for greenhouse gas mitigation to produce syngas. *Molecules* **2022**, *27*, 356.

(37) Ahmad, N.; Alharthi, F.; Alam, M.; Wahab, R.; Manoharadas, S.; Alrayes, B. Syngas production via CO_2 reforming of methane over $SrNiO_3$ and $CeNiO_3$ perovskites. *Energies* **2021**, *14*, 2928.

(38) Valderrama, G.; Goldwasser, M. R.; de Navarro, C. U.; Tatibouët, J. M.; Barrault, J.; Batiot-Dupeyrat, C.; Martínez, F. Dry reforming of methane over Ni perovskite type oxides. *Catal. Today* **2005**, *107-108*, 785−791.

(39) de Lima, S. M.; Assaf, J. M. Ni−Fe catalysts based on perovskite-type oxides for dry reforming of methane to syngas. *Catal. Lett.* **2006**, *108*, 63−70.

(40) Hayashi, H.; Hakuta, Y. Hydrothermal synthesis of metal oxide nanoparticles in supercritical water. *Materials* **2010**, *3*, 3794−3817.

(41) Takesue, M.; Suino, A.; Hakuta, Y.; Hayashi, H.; Smith, R. L., Jr Crystallization trigger of Mn-doped zinc silicate in supercritical water via Zn, Mn, Si sources and complexing agent ethylenediamine tetraacetic acid. *Mater. Chem. Phys.* **2010**, *121*, 330−334.

(42) Assaaoudi, H.; Fang, Z.; Butler, I.; Kozinski, J. Synthesis of erbium hydroxide microflowers and nanostructures in subcritical water. *Nanotechnology* **2008**, *19*, No. 185606.

(43) Sato, T.; Sue, K.; Tsumatori, H.; Suzuki, M.; Tanaka, S.; Kawai-Nakamura, A.; Saitoh, K.; Aida, K.; Hiaki, T. Hydrothermal synthesis of $CuAlO_2$ with the delafossite structure in supercritical water. *J. Supercrit. Fluids* **2008**, *46*, 173−177.

(44) Hayashi, H.; Ueda, A.; Suino, A.; Hiro, K.; Hakuta, Y. Hydrothermal synthesis of yttria stabilized ZrO_2 nanoparticles in subcritical and supercritical water using a flow reaction system. *J. Solid State Sci.* **2009**, *182*, 2985−2990.

(45) Takami, S.; Ohara, S.; Adschiri, T.; Wakayama, Y.; Chikyow, T. Continuous synthesis of organic−inorganic hybridized cubic nano-assemblies of octahedral cerium oxide nanocrystals and hexanedioic acid. *Dalton Trans.* **2008**, 5442−5446.

(46) Kim, J.; Park, Y.-S.; Veriansyah, B.; Kim, J.-D.; Lee, Y.-W. Continuous synthesis of surface-modified metal oxide nanoparticles using supercritical methanol for highly stabilized nanofluids. *Chem. Mater.* **2008**, *20*, 6301−6303.

(47) Bakatula, E. N.; Richard, D.; Neculita, C. M.; Zagury, G. J. Determination of point of zero charge of natural organic materials. *Environ. Sci. Pollut. Res.* **2018**, *25*, 7823−7833.

(48) Qu, Y.; Zhou, W.; Fu, H. Porous cobalt titanate nanorod: A new candidate for visible light-driven photocatalytic water oxidation. *ChemCatChem* **2014**, *6*, 265−270.

(49) Vinogradov, A. V.; Vinogradov, V. V.; Gerasimova, T. V.; Agafonov, A. V. Low-temperature sol-gel synthesis of crystalline CoTiO$_3$ coatings without annealing. *J. Alloys Compd.* **2012**, *543*, 172−175.

(50) Jung, K. Y.; Park, S. B. Effect of calcination temperature and addition of silica, zirconia, alumina on the photocatalytic activity of titania. *Korean J. Chem. Eng.* **2001**, *18*, 879−888.

(51) Baraton, M. I.; Busca, G.; Prieto, M. C.; Ricchiardi, G.; Escribano, V. S. On the vibrational spectra and structure of FeCrO$_3$ and of the ilmenite-type compounds CoTiO$_3$ and NiTiO$_3$. *J. Solid State Chem.* **1994**, *112*, 9−14.

(52) Vásquez, G. C.; Peche-Herrero, M. A.; Maestre, D.; Alemán, B.; Ramírez-Castellanos, J.; Cremades, A.; González-Calbet, J. M.; Piqueras, J. Influence of Fe and Al doping on the stabilization of the anatase phase in TiO$_2$ nanoparticles. *J. Mater. Chem. C* **2014**, *2*, 10377−10385.

(53) Lu, D.; Zhang, G.; Wan, Z. Visible-light-driven g-C$_3$N$_4$/Ti^{3+}-TiO$_2$ photocatalyst co-exposed {001} and {101} facets and its enhanced photocatalytic activities for organic pollutant degradation and Cr(VI) reduction. *Appl. Surf. Sci.* **2015**, *358*, 223−230.

(54) Maensiri, S.; Laokul, P.; Klinkaewnarong, J. A simple synthesis and room-temperature magnetic behavior of Co-doped anatase TiO$_2$ nanoparticles. *J. Magn. Magn. Mater.* **2006**, *302*, 448−453.

(55) Acharya, T.; Choudhary, R. N. P. Structural, dielectric and impedance characteristics of CoTiO$_3$. *Mater. Chem. Phys.* **2016**, *177*, 131−139.

(56) Shen, P. S.; Tseng, C. M.; Kuo, T. C.; Shih, C. K.; Li, M. H.; Chen, P. Microwave-assisted synthesis of titanium dioxide nanocrystalline for efficient dye-sensitized and perovskite solar cells. *Sol. Energy* **2015**, *120*, 345−356.

(57) Thommes, M.; Kaneko, K.; Neimark, A. V.; Olivier, J. P.; Rodriguez-Reinoso, F.; Rouquerol, J.; Sing, K. S. W. Physisorption of gases, with special reference to the evaluation of surface area and pore size distribution (IUPAC Technical Report). *Pure Appl. Chem.* **2015**, *87*, 1051−1069.

(58) Liu, Y.; Shen, B.; Yang, Z.; Zhao, P. Pore structure characterization and the controlling factors of the bakken formation. *Energies* **2018**, *11*, 2879.

(59) Zhou, W.; Fu, H. Mesoporous TiO$_2$: Preparation, doping, and as a composite for photocatalysis. *ChemCatChem* **2013**, *5*, 885−894.

(60) Nguyen, D. T.; Ha, C. A.; Nguyen, T. Controlling phase composition, properties and activity of TiO$_2$ nano-photocatalyst synthesized by hydrothermal technique in the degradation of cinnamic acid solution. *J. Nanosci. Nanotechnol.* **2020**, *20*, 5418−5425.

(61) Dey, S.; Ricciardo, R. A.; Cuthbert, H. L.; Woodward, P. M. Metal-to-metal charge transfer in AWO$_4$ (A = Mg, Mn, Co, Ni, Cu, or Zn) compounds with the wolframite structure. *Inorg. Chem.* **2014**, *53*, 4394−4399.

(62) Xu, Y.; Schoonen, M. A. A. The absolute energy positions of conduction and valence bands of selected semiconducting minerals. *Am. Mineral.* **2000**, *85*, 543−556.

(63) Wangkawong, K.; Phanichphant, S.; Tantraviwat, D.; Inceesungvorn, B. CoTiO$_3$/Ag$_3$VO$_4$ composite: A study on the role of CoTiO$_3$ and the active species in the photocatalytic degradation of methylene blue. *J. Colloid Interface Sci.* **2015**, *454*, 210−215.

(64) Li, M. W.; Yuan, J. P.; Gao, X. M.; Liang, E. Q.; Wang, C. Y. Structure and optical absorption properties of NiTiO$_3$ nanocrystallites. *Appl. Phys. A: Mater. Sci. Process.* **2016**, *122*, No. 725.

(65) Xu, H.; Yan, J.; Xu, Y.; Song, Y.; Li, H.; Xia, J.; Huang, C.; Wan, H. Novel visible-light-driven AgX/graphite-like C$_3$N$_4$ (X=Br, I) hybrid materials with synergistic photocatalytic activity. *Appl. Catal., B* **2013**, *129*, 182−193.

(66) Jamil, M.; Khan, Z. S.; Ali, A.; Iqbal, N. Studies on solution processed Graphene-Nb$_2$O$_5$ nanocomposite based photoanode for dye-sensitized solar cells. *J. Alloys Compd.* **2017**, *694*, 401−407.

(67) Reddy, C. V.; Babu, B.; Reddy, I. N.; Shim, J. Synthesis and characterization of pure tetragonal ZrO$_2$ nanoparticles with enhanced photocatalytic activity. *Ceram. Int.* **2018**, *44*, 6940−6948.

(68) Wang, C.; Wu, D.; Wang, P.; Ao, Y.; Hou, J.; Qian, J. Effect of oxygen vacancy on enhanced photocatalytic activity of reduced ZnO nanorod arrays. *Appl. Surf. Sci.* **2015**, *325*, 112−116.

(69) Rezaei-Vahidian, H.; Zarei, A. R.; Soleymani, A. R. Degradation of nitro-aromatic explosives using recyclable magnetic photocatalyst: Catalyst synthesis and process optimization. *J. Hazard. Mater.* **2017**, *325*, 310−318.

(70) He, H. Y.; Huang, J. F.; Cao, L. Y.; Wu, J. P. Photodegradation of methyl orange aqueous on MnWO$_4$ powder under different light resources and initial pH. *Desalination* **2010**, *252*, 66−70.

(71) Grimes, S. M.; Mehta, L. K.; Ngwang, H. C. Photocatalytic degradation of trans-cinnamic, dihydrocinnamic, trans-caffeic, and dihydrocaffeic acids and characterization of the products. *J. Environ. Sci. Health, Part A* **2001**, *36*, 599−612.

(72) Madureira, J.; Barros, L.; Melo, R.; Cabo Verde, S.; Ferreira, I. C. F. R.; Margaça, F. M. A. Degradation of phenolic acids by gamma radiation as model compounds of cork wastewaters. *Chem. Eng. J.* **2018**, *341*, 227−237.

(73) Moghiminia, S.; Farsi, H.; Raissi, H. Comparative optical and electrochemical studies of nanostructured NiTiO$_3$ and NiTiO$_3$-TiO$_2$ prepared by a low temperature modified sol-gel route. *Electrochim. Acta* **2014**, *132*, 512−523.

(74) Wang, Q.; Guo, Q.; Wang, L.; Li, B. The flux growth of single-crystalline CoTiO$_3$ polyhedral particles and improved visible-light photocatalytic activity of heterostructured CoTiO$_3$/g-C$_3$N$_4$ composites. *Dalton Trans.* **2016**, *45*, 17748−17758.